Final Draft

of the original manuscript

Hassenkam, T.; Tsai, E.; Sørensen, H.; Dalby, K.; Mackenzie, D.; Holler, M.; Ferreira, D.; Grolimund, D.; Bruns, S.; Rosing, M.:
Direct evidence for eoarchean iron metabolism?.
In: Geobiology. Vol. 19 (2021) 3, 218 - 227.

First published online by Wiley-Blackwell: 24.02.2021

https://dx.doi.org/10.1111/gbi.12432

Direct Evidence For Eoarchean Iron Metabolism?

Tue Hassenkam*[1], Esther H. R. Tsai[2,3], Henning O. Sørensen[4,5], Kim N. Dalby[4,6], David M. A. Mackenzie[7], Mirko Holler[2], Dario Ferreira[2], Daniel Grolimund[2], Stefan Bruns[4], Minik T. Rosing[1]

1. Globe institute, University of Copenhagen, DK-2100, Denmark

2. Paul Scherrer Institut, 5232 Villigen PSI,Switzerland

3. Center for Functional Nanomaterials, Brookhaven National Laboratory, Upton, NY 11973, USA

4. Nano-Science Center, Department of Chemistry, University of Copenhagen, DK-2100 Copenhagen Ø, Denmark

5. Department of Physics, Technical University of Denmark, Kongens Lyngby, 2800, Denmark

6. Haldor Topsøe A/S, Haldor Topsøes All\'e 1, DK-2800 Kgs. Lyngby, Denmark

7. Department of Electronics and Nanoengineering, Aalto University, PO Box 13500, FI-00076 Aalto, Finland

*Correspondence to: tue.hassenkam@sund.ku.dk

Abstract

Metasedimentary rocks from Isua, West Greenland (> 3,700 million years old) contain carbonaceous compounds, compatible with a biogenic origin (Hassenkam, Andersson, Dalby, Mackenzie, & Rosing, 2017; Ohtomo, Kakegawa, Ishida, Nagase, & Rosing, 2014; Rosing, 1999). The metamorphic mineral assemblage with garnet and quartz intergrowths contains layers of carbonaceous inclusions contiguous with carbon-rich sedimentary beds in the host rock. Previous studies (Hassenkam et al., 2017; Ohtomo et al., 2014; Rosing, 1999) on Isua rocks focused on testing the biogenic origin of the carbonaceous material, but here we searched for evidence which could provide new insights into the nature of the life that generated this carbonaceous material. We studied material trapped in inclusions armoured within quartz grains inside garnet porphyroblasts by non-destructive ptychographic X-ray nanotomography (PXCT). The 3D electron density maps generated by PXCT were correlated with maps from X-ray fluorescence tomography and micro-Raman spectroscopy. We found that the material trapped inside inclusions in the quartz grains consist of disordered carbon material encasing domains of iron-rich carbonaceous material. These results corroborate earlier claims (Hassenkam et al., 2017; Ohtomo et al., 2014; Rosing, 1999) for biogenic origins and are compatible with relics of metamorphosed biological material originally containing high iron/carbon ratios, comparable to ratios found in most extant organisms. These iron-rich domains represent the oldest evidence for organic iron complexes in the geologic record and is consistent with Fe-isotopic evidence for

metabolic iron fractionation in >3700 Ma Isua banded iron formation (Czaja et al., 2013; M. J. Whitehouse & C. M. Fedo, 2007)

Introduction

Metabolism is one of the fundamental pillars of life. While the morphology of unicellular lifeforms is mostly unspecific and not unique to life, metabolism is a suite of highly selective processes catalysed by life, which cause systematic and specific environmental changes. These changes are preserved in the chemical and isotopic composition of sedimentary rocks. The earliest traces of life on Earth consist of metamorphosed carbonaceous compounds, which have isotopic (Ohtomo et al., 2014; Rosing, 1999; Whitehouse, Dunkley, Kusiak, & Wilde, 2019; Martin J. Whitehouse & Christopher M. Fedo, 2007), chemical and structural (Hassenkam et al., 2017; Ohtomo et al., 2014) characteristics compatible with a biogenic origin. Collectively, a high and continuous rate of deposition of reduced carbon in a marine environment, a consistent, monotonous ^{13}C depletion of the reduced carbon across the stratigraphic section (Rosing & Frei, 2004), and the presence of nitrogen and phosphate chemically bound to carbon (Hassenkam et al., 2017), only support a biological source of the reduced carbon.

It has been proposed that iron was an essential component in early microbial metabolic redox chemistry (Vargas, Kashefi, Blunt-Harris, & Lovley, 1998; Widdel et al., 1993). Eoarchean oceans had high levels of dissolved iron (40-120μM) (Canfield, 2005) and oxygen was very low (Kasting, 1993; Vargas et al., 1998; Walker, 1987), in contrast to modern oceans where the levels of dissolved iron is low (1 μM) (Armstrong, 1957), and oxygen is high. Many extant organisms use iron, e.g. ferric iron for respiration (Kashefi & Lovley, 2003; Vargas et al., 1998), ferrous iron for aerobic lithotrophic iron oxidation and ferrous iron as an electron donor in

anoxygenic photosynthetic iron oxidation (Kashefi & Lovley, 2003; Widdel et al., 1993). It is assumed that iron-based metabolism is deeply rooted in life (Beard, Dawson, & Piñero, 1996; Neilands, 1974). Most iron in Earth's extant surface environments is ferric, Fe(III), and bound in oxyhydroxides, which are insoluble in water and therefore not readily available to life. Even so, many essential functions of life still depend on iron today (Beard et al., 1996; Drakesmith & Prentice, 2012; Earhart, 2009). This includes ATP, DNA and protein synthesis (Aisen, Enns, & Wessling-Resnick, 2001), compatible with the dependence of iron and iron compounds being deeply rooted in the tree of life (Beard et al., 1996; Neilands, 1974). Therefore, the availability of iron may have been a critical element for early proliferation of life (de Duve, 1990). In this study, we searched for structural and chemical evidence linking iron in the sediments to the organisms responsible for the carbonaceous components.

The Isua supracrustal belt is the largest and least reworked contiguous relic of Eoarchean supracrust, i.e. shallow volcanic and sedimentary rocks. The metasedimentary package forms a ca. 30 km long and up to 4 km wide arcuate belt within the Itsaq gneiss complex of West Greenland (Nutman, McGregor, Friend, Bennett, & Kinny, 1996) (Fig. 1a). All parts of the belt have experienced amphibolite facies metamorphism, but strain has been heterogeneously distributed. This has allowed for the preservation of small domains (tens to hundreds of meters) in which primary features such as sedimentary bedding, volcanic pillow structures and vesicles and varioles are preserved. Near the North-Eastern termination of the belt, a sedimentary sequence dominated by Bouma sequence turbidites and black shales intercalated with basaltic volcanic rocks and banded iron formation has been identified (Rosing, 1999) (Fig. 1b). The rocks have undergone amphibolite facies metamorphism, locally with no or only minor strain. The sedimentary bedding as well as the metamorphic mineral fabric has been intruded

by cross cutting felsic igneous sheets, which contain 3700 Ma magmatic zircons (Nutman & Friend, 2009). Radiogenic isotope systems place the age of the metasediments in the Early Archean/Eoarchean period, but with large uncertainties in the 100 Ma range. Thus, we can only say that the rocks were deposited and metamorphosed > 3700 Ma ago, pinned by the age of the cross cutting felsic sheets and consistent with the isotopic composition of the rocks themselves (Rosing, 1999). Pelitic shales and iron rich pelites, transitional between BIF and pelitic shales preserve sedimentary bedding, preserved as mm to sub-mm scale compositional layering in the metasediment. Some of these layers are rich in carbonaceous material, mostly graphite, which is strictly bound to the sedimentary bedding (Fig. 1c). In the iron-rich pelites, millimetre sized garnet porphyroblasts have formed, which have overgrown parts of the compositional layering. The sedimentary bedding planes are outlined by planar inclusion trails inside the garnet crystals (Fig. 1c). The very resilient garnet crystals have not experienced very minor detectable deformation, since they formed 3700 Ma ago, although, in places, they were slightly rotated relative to the more ductile matrix by later shear deformation. Garnet crystals are very robust and inclusions preserved inside garnets are well protected from leakage of fluids from the inclusions or chemical interaction with transient metamorphic fluids from the country rock.

The samples studied here show trails of carbonaceous particles forming micrometre sized inclusions across the metamorphic minerals that have replaced the protolith sediment (Fig. 2a, b). The trails are contiguous across mineral boundaries including across quartz inclusions found inside garnets (Fig. 2b). Closer inspection with scanning electron microscopy (SEM) (Fig. 2c) with energy-dispersive X-ray spectroscopy (EDXS) (Fig. S1) reveals that inclusions inside the quartz inclusions contain carbon rich material (arrowhead Fig. 2c). We have isolated such a quartz grain (see methods) and analysed the set of inclusions trapped inside using non-destructive methods. Fig. 3a displays an optical image of the particle, and since quartz is

optically transparent, the black carbonaceous inclusions are easily discernible (indicated by red arrow).

The internal 3D structure of the sample was revealed through Ptychographic X-ray computed tomography (PXCT) (Dierolf et al., 2010; Holler, Guizar-Sicairos, et al., 2017) at cSAXS, Swiss Light Source. This is first time this has been done on such samples. The quartz particle was mounted on a sample holder designed for PXCT (Holler, Raabe, et al., 2017) (Fig. 3b). EDXS of the particle confirmed that it is mainly silicon and oxygen, which we interpret to be quartz (Fig. 3c). Fig. 3d shows a 3D electron density map obtained by PXCT (Movie in online data) of the inclusions, while Fig. 3e-g show 2D orthogonal slices of the quartz inclusion, where the cross point between the slices was chosen to be inside the inclusions and Fig. 3h shows a 1D electron density profile across the inclusions in Fig. 3e. The particle was painted with a thin strip of platinum during sample preparation, giving rise to the high electron density light grey seen on the top part of the grain in Fig. 3e. Inside the bulk of the particle the electron density was generally uniform at around 0.80 e/Å^3, which is consistent with quartz (Diaz et al., 2012). Inside the row of inclusions the electron density value was approximately 0.67 e/Å^3 consistent with carbonaceous material (Diaz et al., 2012). The tomograms revealed a set of internal domains enclosed within the carbonaceous material with an electron density around 0.9 e/Å^3, which is higher than both that of carbonaceous material and quartz. These internal domains, which are irregular in shape and roughly from 50 nm to 800 nm across, will be referred to as High Electron Density (HED) domains. To verify that the inclusions shown here were not just a statistical fluke we confirmed the presence of similar features in 129 inclusions among 36 other samples (18 examples shown in Fig. S2) using nanotomography at BL47XU, SPring-8 in Japan. To learn more about the structural composition of the carbonaceous material inside the inclusions with HED domains we analysed the sample using micro-Raman spectroscopy.

Micro-Raman-spectra obtained with the focal point inside the inclusions showed a profile consistent with quartz and amorphous carbon (Fig. 4a) with the characteristic G (graphite)-peak around 1580 cm^{-1} and D (defect) peak around 1350 cm^{-1}. A micro-Raman spectroscopy map collected across the particle, where we show the position of the G-peak (ω_G) (Fig. 4c) confirmed that the carbon signal coincided only with the position of the inclusions. The ω_G varied between 1585 and 1610 cm^{-1} with an average of 1595 cm^{-1} (Fig. S3). The upshift in ω_G from 1580 cm^{-1} of pure graphite is characteristic with a high degree of disorder in the carbonaceous material that gives rise to overlaps between G-peaks and D-peaks, which could shift the apparent location of the G-peak in the Raman spectra but it can also be consistent with the presence of nitrogen and oxygen bound to the carbon material (Khai et al., 2012; Paulose, Raghavan, & George, 2016). In a previous study (Hassenkam et al., 2017) on graphitic material from the same rocks we found oxygen and nitrogen bound to carbon by IR spectroscopy. This was consistent with Raman spectroscopy that showed a variation of the G-peak on the order of 10 cm^{-1}, consistent with graphite bonded to nitrogen or oxygen. The ratio between the intensity of the G-peak and the D-peak is another indicator for graphite structural disorder (Ferrari & Robertson, 2000). The map of ratios shown in Fig. 4d, has an average value around 0.5, suggesting that the carbonaceous material inside the inclusions is a mixture of highly disordered amorphous carbon and possibly a small amount of nano-crystalline graphite (Ferrari & Robertson, 2000). In our previous study we observed that the carbonaceous material in these samples was found to be either purely graphitic or highly disordered (Hassenkam et al. 2017). The highly disordered carbonaceous material was only found amoured inside garnet crystals, while the continued trails of carbonaceous inclusions which continued into the surrounding rock matrix, showed highly graphitic material. This is consistent with the current

sample where the carbonaceous material is inside a quartz crystal that was trapped inside a garnet crystal. We are not the first to find such highly disordered carbonaceous material preserved in very old rock samples. Dutkiewicz *et al.* (Dutkiewicz, Rasmussen, & Buick, 1998) have shown that 3 billion year old rocks can preserve highly disordered liquid carbonaceous material inside small inclusions.

While the Raman micro-spectroscopy could confirm the presence of carbonaceous material inside the inclusions, give an idea about the structural integrity of the carbonaceous material and hint to the presence of other elements, it could not specifically identify any non-carbon element(s) in the HED domains. The tomography showed that the electron density of the HED domains is higher than that of both carbon and SiO_2, they must therefore contain heavier elements than the surrounding carbon. To identify these heavier elements, we employed X-ray fluorescence tomography.

Fig. 5a shows orthogonal views of the electron density tomography data, but now with a full view of the particle. The colour scale was chosen to emphasize the HED domains (red). Fig. 5b shows the corresponding X-ray fluorescence tomography data with slices positioned approximately with the same orientation and positions as the slices shown in Fig. 5a. X-ray fluorescence, on samples thicker than 1 μm, can only detects elements heavier than Si, this means it cannot detect elements like carbon or oxygen. The spatial resolutions provided by the two techniques are quite different. The voxel size of the electron density tomography map is 21.47 nm, while it is 500 nm for the fluorescence maps. Hence a slice of the fluorescence maps is substantially thicker than the corresponding PXCT slice. Nevertheless, comparing the set of slices in Fig. 5a with the set of slices shown in Fig. 5b it is evident that the position of the

inclusions carrying HED domains correlate with areas of increased iron concentration. The concentration of silicon decreases where iron increases. Combined with the observation that the electron density of material surrounding the HED inclusions match that found for almost pure amorphous carbon, means that the iron must be concentrated inside the HED domains. But the electron density of 0.9 e/Å^3 is well below that of pure iron (2.2 e/Å^3), this means that there is only a fraction of the material inside the HED is iron. To determine this fraction is, and maybe the identity of the HED domains, we will use the proportionality between the electron density and material density expressed by:

$$\rho = \frac{n_e A}{Z N_A}, \quad (1)$$

Where ρ is the material density, n_e is the electron density, A is the molar mass, Z is the number of electrons and N_A is Avogadros number. For most lighter atoms the ratio A/Z is 2, for iron it is 2.1. this means that material density scales linearly with the electron density for the same material composition. Using 0.67 e/Å^3 for the carbonaceous material gives a density around 2.2 g/cm^3 consistent with dense carbon. The 0.9 e/Å^3 would therefore correspond to a material density of about 3.0 g/cm^3, assuming a A/Z ratio of 2. We can use this material density as determining parameter and try to combine Fe with elements lighter than Si, since Si is not detected inside the inclusions. Two of these lighter elements stand out: oxygen and carbon. Oxygen because iron easily forms stable iron oxide compounds and carbon because the iron rich domains are embedded in carbonaceous material. Using the material density of 3.0 g/cm^3 as the determining parameter the HED domains do not match that of pure iron (7.8 g/cm^3), iron carbide (4.93 g/cm^3), garnet (the host mineral outside the quartz particle), almandine, 4.19 g/cm^3), iron oxides (magnetite (5.2 g/cm^3), hematite (5.3 g/cm^3) or wüstite (5.7 g/cm^3).

Another possibility is the family of green rust compounds which are a mixed-valence Fe(II),Fe(III)-layered hydroxide compounds with intercalated anions, such as carbonate, sulfate, chloride etc. Most of these have mass densities below 3 g/cm^3, e.g. the green rust sodium sulfate has a density of 2.3 g/cm^3 and its electro density is 0.72 e/Å^3(Christiansen et al., 2009), so they cannot by themselves match the observed for HED, and we do not detect sulfate, chloride etc. in the inclusions either. It does not fit pure Iron(II) compounds like Iron(II) hydroxide (3.4 g/cm^3) either. Nor does it fit the most obvious combination of carbon, iron and oxygen, siderite (3.96 g/cm^3). More exotic combinations with other lighter elements iron(III)fluoride (3.87 g/cm^3) or sodium ferrioxalate (1.97 g/cm^3) for instance does not have a density that match the observed value. The tabular particles seen in the top part of the side view in Fig. 5a, external to the carbonaceous material, contain iron, potassium and titanium (Fig. 5c), aluminium (EDXS data not shown) consistent with biotite (3.1 g/cm^3), which is abundant in the rock matrix. The level of the iron signal for the biotite was on par with the level for HED domains but no potassium or titanium has been detected in the HED (Fig. 5c). We have only detected iron and carbonaceous material inside the inclusions. If we therefore assume that there is mainly carbon and iron inside the HED we can estimate the ratio of iron relative to carbon by calculating the amount of iron needed in the carbon matrix to reach the increased electron density. If we assume that the iron is bound in tiny BCC (Body-Centered-Cubic) crystals, the electron density of those crystals would be 2.2 e/Å^3 using equation 1. Assuming the linearity of equation 1 the relative amount x of BCC iron in the HEDs can be estimated by $n_{HED} = (1-x)*n_c + x*n_{iron}$ or $x = (n_{hed}-nc)/(n_{iron}-n_c)$. This amounts to 14.8% by volume of the carbon being replaced by iron in the HED domains when compared to the surrounding carbon. Assuming that the iron is bound in BCC crystals and using the material density of 7.8 g/cm^3 for iron and 2.2 g/cm^3 for the carbonaceous material the iron within 1 cm^3 of HED material would

amount to 0.148*7.8 g/cm^3= 1.15 g, while the carbon would amount to 0.852*2.2=1.87 g. Translating this into numbers of atoms means that 1 cm^3 of HED material would contain 0.156 mol carbon and 0.02 mol iron, or roughly 8 carbon atoms for every iron atom. However, this is assuming that the iron is bound in BCC crystals. There is no direct evidence to support this assumption but the homogeneity of the HED domains suggest that the iron is not forming small isolated mineral crystals, but is evenly dispersed in the HED domains. If the iron was bound in small mineral grains the size would have to be much less than the voxel size (around 10 nm) in order to match the density found and for the mixed phases not to show up in the tomography data. The mineral grains would also have to be perfectly mixed across the whole HED and be mixed with same proportions in separate domains. We find this highly unlikely and it is also inconsistent with the fundamental instability of nano crystalline particles.

If indeed the iron is bound in small mineral grains, it would mean that there would be a thermodynamic drive for separation of carbon compounds and iron compounds. Given time, Ostwald ripening would cause smaller iron particles to coalesce into larger particles. The logical consequence of this, given the huge timespan in question and the apparent disordered phase of the carbon, is either the iron is bound in large iron oxide mineral grains, that would be visible in the tomography, or it is molecular bound to the carbon material possibly through oxygen.

If we therefore, instead assume that iron atoms are replacing carbon atoms in isolated locations in the carbon matrix, the calculation is slightly different. Then we would have to estimate the number of electrons added whenever a carbon is replaced by an iron atom. We should also have to take into account how much space an iron atom takes up relative to a carbon atom, but assuming that when iron is bound either as Fe(II) or Fe(III) the volume is about the same and finding the fraction iron atoms x is then given by:

$$\frac{0.9}{0.67} = \frac{6(1-x)+26x}{6}$$

x then becomes 10% or 1 iron atom for every 9 carbon atoms. The ratio would vary slightly depending on the amounts of lighter atoms present in the inclusions. Elements like oxygen and hydrogen could not be detected by the X-ray fluorescence tomography. We have assumed that while the electron density data and Raman suggest mainly carbon any traces of oxygen and hydrogen is roughly evenly distributed across all the carbonaceous material including the HED domains, and the relative ratio above would therefore be unaffected by the presence of oxygen and hydrogen. Nevertheless, it would be reasonable to assume that there would be slightly more oxygen with the iron. If there on average was one extra oxygen for each iron the ratio would then change approximately to 1 iron for every 8 carbon atoms, since the change in the overall density when replacing one out of 10 carbon atom with oxygen is only around 2-3%.

For the cluster of inclusions shown in Fig. 3-5, the volume ratio between the carbonaceous material and the HED domains is around 2%, meaning that the rest of volume (98%) is the pure carbonaceous material distributed in inclusions across the whole particle. One iron atom per 9 carbon atoms in the HED domains therefore translate into an iron content of 0.9% of dry weight, relative to all carbon integrated over the entire cluster of inclusions, which also includes the pure carbonaceous inclusions in the particle. The concentration of iron in the inclusions are several orders of magnitude higher than a simple equilibrium with the ancient ocean environment would dictate (assuming trapped water volume of approximately 5 times that of the inclusion with 120 μM dissolved iron).

The geological data is not consistent with the carbon or the iron being introduced into the rock formation by some later process. The sedimentary rock themselves form part of a supracrustal

sequence which experienced amphibolite facies metamorphism sometime during the early Archean and before emplacement of felsic igneous sheets of the Amitsoq gnies suite at 3700 Ma, and also before emplacement of the mafic so-called Ameralik dikes at 3510 Ma. This is based on undeformed igneous bodies crosscutting the metamorphic fabric of the metasedimentary rocks. The field occurrence of the samples studied here is a rare low-deformation augen in the Isua complex, where sedimentary bedding is still preserved. The carbonaceous particles are solely found in inclusions inside metamorphic garnet porphyroblasts, where they have overgrown trails of carbonaceous material in the layered pelitic metasediments, thereby preserving some of the carbonaceous material. The carbonaceous material outside the garnet crystals now consist of well crystallized graphite. Based on this, we deduct that all the carbonaceous material originated as poorly ordered carbonaceous material that formed part of the sediment deposited in the sea 3700 Ma ago, now recrystallized to graphite except where armored by garnet. The elemental ratio of carbon and iron have therefore likely been preserved inside the garnet and we find it highly unlikely that some later processes could have placed and dispersed iron centrally inside domains inside carbonaceous inclusions. And as already discussed the lack of iron mineral grains in the HED suggest that the iron was dispersed in a stable form inside a carbon matrix at the time of the formation of the garnets. Any abiotic process would therefore have to account for a production and deposition of reduced carbon in the sea, with an isotopic ratio consistent with biogenic material and with the set of structurally bound elements (Nitrogen, phosphorous and oxygen) also consistent with biogenic remains. We have not been able to identify a possible set abiogenic processes that would produce carbonaceous material with this set of features.

A biogenic origin for this carbonaceous material, is therefore consistent with the previous published data on the material, but does it also fit this new observed iron data? The presence

of high concentrations of iron, evenly dispersed inside the HED domains, together with the HED domains being enveloped by carbonaceous material, does not agree with post-mortem iron-mineralization. According to Lepot *et al* (Lepot et al., 2017) microfossils that are deposited in iron rich fluids are often encrusted by iron or iron-mineral particles are attached to the outside of the fossils, since the iron precipitates at the cell wall of the decaying microorganisms. The iron found in connection with microfossils deposited in an iron rich environment is therefore often found next to or outside the carbon domains. Here we find the iron dispersed inside the HED domains in C/Fe ratio of around 9:1, which is on the same order of magnitude as some biological molecules such as siderophores (Bazylinski & Frankel, 2004). Examples of smaller siderophores cover compounds like deoxymugineic acid (C/Fe=10/1) or rhodotorulic acid (C/Fe=14/1), while larger compounds like enterobactin (E. coli) with (C/Fe=30/1) or protoporphyrin (C/Fe=34) are more common. However the 0.9% iron in dry weight is about two orders of magnitude higher than what is observed in modern organisms (Abbaspour, Hurrell, & Kelishadi, 2014), like *E. Coli*, a common prokaryote, where the iron content is 0.02% of dry weight (Hartmann & Braun, 1981). The content is much less however, than what is observed in organisms that harvest and store iron for some purpose including some bacteria that store iron for respiration reserves (Luef et al., 2013) or magnetotactic bacteria (Blakemore, 1975; Farina, Esquivel, & de Barros, 1990), which have an iron content around 3% of dry weight (Blakemore, 1975). The iron in the magnetotactic bacteria is stored in small magnetite mineral grains, and since we do not see mineral grains, a direct comparison here is not valid.

The combined observations indicate that putative host organisms had higher partial mass density of iron than required for enzymes in common extant organisms. In addition, the concomitant deposition of reduced carbon and oxidised (ferric) iron, now forming parts of the Isua metasediments, indicates that a process causing chemical disequilibrium was active in the

source of the sediment. This is compatible with a biogenic process, as also concluded by (Czaja et al., 2013), and (M. J. Whitehouse & C. M. Fedo, 2007), based on Fe-isotope fractionation observed in Isua banded iron formations. Here we document an intimate link between the carbon and iron in clastic pelitic metasediments, and propose that iron was involved in metabolic redox chemistry. This could have been mediated by organisms using a photosynthetic metabolic strategy (Fedo, Whitehouse, & Kamber, 2006; Rosing & Frei, 2004) with dissolved ferrous iron as the electron donor, and providing solid ferric iron bearing metabolites as well as organic matter to the sediment.

Even if the ratio of Fe to C might have been altered during metamorphism, several characteristics of these inclusions are consistent with biogenic iron: First the order of magnitude in iron content is within range or slightly higher, than what is found in modern organisms. Secondly, the iron is distributed evenly in carbonaceous domains that are enveloped by iron free amorphous carbon. Thirdly, the size of the cluster of inclusions shown in Fig. 3 and other inclusions similar to these (Fig. s3) is compatible with the size of single cell organisms, and lastly the micro-Raman is consistent with disordered carbonaceous material bound to other elements.

Several studies have confirmed that the part of the Isua rock from which our sample was extracted, contain remains of Eoarchean life (Hassenkam et al., 2017; Rosing, 1999). Our result therefore corroborates these earlier claims, and our potential findings of 3.7-billion-year-old microbial remains being the oldest direct evidence for organisms that used iron in some capacity for their metabolism either as enzymatic catalyst or as a metabolic agent.

Figure list:

Figure 1: Geological setting and map. a) Geological map of the Isua Supracrustal Belt (ISB) in West Greenland. The samples were extracted from the area framed by the black rectangle. b) Bouma sequence alternating pelagic shales and turbiditic psamites. The iron-rich lithologies of this study have been sampled ca. 4 metres along strike from this outcrop from the lower (left-hand) part of the sequence. c) Optical transmission picture of a polished thin section showing typical garnet crystals (one is shown as the bright crystal in the middle of the image) inside the 3,700 million year old metasedimentary rock. The lines of inclusions (dark bands) containing carbonaceous material within the garnet roughly follow the direction of the sedimentary layering.

Figure 2: Carbon inclusions inside quartz inclusions in garnets. a) Thin section of the Isua metasediment seen in cross-polarized transmitted light. The trails of carbon material are contiguous across mineral particles. b) The same area as a) but in reflected light. The bright particles are garnets and the darker quartz inclusions are inside garnets. One of these quartz inclusions are indicated by the red arrow. c) Scanning electron microscopy image of a fractured garnet surface. Trails of inclusions containing carbonaceous material are found inside the garnet and continue inside a quartz inclusion inside the garnet (red arrow).

Figure 3: Quartz particle containing carbonaceous inclusions. a) Optical image seen from above. The red arrowhead indicates the top visible part of the carbonaceous material trapped inside the quartz particle. b) Scanning electron microscopy image of the particle seen from the side mounted by Pt strips onto a Omniprobe needle. c) EDX spectra of the particle. d) A

rendering of the 3D electron density map extracted from ptychographic tomography showing the trail of carbonaceous inclusions (translucent black) with HED domains shown in solid red. e-f) Orthogonal slice view of the electron density across the inclusions with HED domains being the bright (high-electron-density) regions inside the inclusions. h) The electron density profile across the inclusion as indicated by the blue line in e). EDXS spectrum at spots where the inclusions was close to the surface are shown in Fig. S4

Figure 4: Raman micro-spectra of the particle with inclusions shown in Fig. 3. The focal plane was chosen to be where the inclusions were most dense. a) A representative spectrum showing the characteristic D (at approx. 1350 cm^{-1}) and G peaks (at approx. 1590 cm^{-1}) for graphite, alongside the quartz peaks (below 500 cm^{-1}) . b) The optical image of the sample seen from the top. c) The variation in the position of the G-peak (ω_G) across the sample. In the white areas correspond to areas were no G-peak could be fitted. d) The ratio between the intensities of the G and D peaks.

Figure 5: Correlated PXCT and X-ray fluorescence maps of the quartz particle. a) Orthogonal electron density maps with cross-point inside the inclusions. The maps have been falsely coloured to emphasise regions with similar electron density (carbonaceous material in light blue and HED domains in red). b) Orthogonal X-ray fluorescence maps with fluorescence consistent with silicon (Si), iron (Fe) and platinum (Pt) overlaid a single slice with approximately the same position and orientation as shown in a). c) Same as b) but with potassium (K), iron (Fe) and titanium (Ti). A fully indexed XRF spectrum for the whole sample is shown in Fig. S5

410

Materials and Methods:

SEM: A dual beam FEI Quanta 3D focused ion beam scanning electron microscope (FIBSEM) was used to prepare the sample for tomography and to provide energy dispersive X-ray
415 spectroscopy (EDXS) data. First a garnet was cracked between two clean glass slides, a suitable crystal extracted by AFM in the optical microscope and transferred to the SEM. Using an OmniProbe micromanipulator, the crystal was transferred to the custom cSAXS beamline PCXT sample holder. Small strips of platinum were used to attach the quartz to the OmniProbe needle and subsequently the sample holder (deposited using a gas injection system GIS)) and a Ga ion
420 beam was used to remove the grain from the OmniProbe needle. A voltage contrast detector and Oxford X-max 20 mm^2 X-ray spectrometer was used to collect the SEM EDXS data. The samples were not coated, but instead were analysed under low vacuum (60 Pa) conditions, to minimize charging. Water vapour was used to maintain vacuum. The images and EDXS were performed using an accelerating voltage of 10 kV and probe current of 8 nA.

425

Micro-Raman spectroscopy:

was performed using a Thermo Scientific DXRxi with a 532 nm laser, 10 mW laser power, a 100x objective with numerical aperture of 0.80, resulting in a spot size of 600 nm. Maps were performed by stepping the sample stage with 200 nm increments in order to achieve spatial
430 oversampling from the diffraction limited laser spot and with an integration time of 0.0556 s, and 100 scans per pixel. The map was repeated 20 times for different z-focuses, with the focus of the first map at the top of the inner inclusion and each subsequent map being focused an

additional 500 nm lower. A total of 165,600 spectra were collected. The position, width and relative intensities of the G and D peaks were extracted using standard fitting methods (Larsen, Mackenzie, Caridad, Bøggild, & Booth, 2014). Pixels where an adequate fit was not achieved are set to white in Fig. 4. The setup with similar laser power had previously been used on graphitic material and no evidence for degradation (increase in D-peak) was observed, so we can exclude beam damage from the laser.

Ptychographic X-ray computed tomography (PXCT):

PXCT (Dierolf et al., 2010) experiments were performed at the cSAXS beamline (X12SA) of the Swiss Light Source (SLS), Paul Scherrer Institut, Switzerland. The 3D imaging method offers quantitativeness (Diaz et al., 2012) with nanoscale resolution (Holler et al., 2014; Holler, Guizar-Sicairos, et al., 2017). A 6.2 keV illumination was defined by a double crystal Si(111) monochromator. A gold central beam stop was placed upstream the Fresnel zone plate (FZP) (Gorelick et al., 2011) and an order sorting aperture was mounted downstream near the focus. The FZP had an outer zone width of 60 nm and a diameter of 170 μm and the central stop had a diameter of 40 μm, both of which were fabricated in the Laboratory for Micro and Nanotechnology, Paul Scherrer Institut, Switzerland. The sample was mounted on a customized sample pin (Holler, Raabe, et al., 2017) by FIB and placed a few mm off the focus to have a illumination with a diameter of around 5 μm. Following the Fermat spiral pattern (Huang et al., 2014), the mounted sample was scanned over a field of view of 40 μm horizontally and 20 μm vertically. For each scanning point, a diffraction pattern was recorded 7.4 m downstream of the object using a Pilatus 2M detector (Henrich et al., 2009) with an exposure of 0.1 sec. The object pixel size was 21 nm, based on the diffraction pattern size (i.e. 400x400 pixels) used for the

reconstructions algorithms (Thibault et al., 2008; Thibault & Guizar-Sicairos, 2012). A scanning step size of roughly 1.2 μm was used and 460 projections were taken, achieving an estimated 3D resolution of 75 nm based on the Fourier Shell Correlation (FSC) (van Heel & Schatz, 2005).

X-ray fluorescence tomography

Scanning X-ray fluorescence data were collected at the microXAS beamline (X05LA), SLS, Paul Scherrer Institut, Switzerland. Imaging was carried out at 7.3 keV to map the elements in the sample, e.g. Fe. A few spectres was collected at 17.2 keV (not shown) to screen for other heavier elements and confirm the presence of Pt. The incident pencil beam was focused to 1 μm^2 through a Kirkpatrick-Baez (KB) mirror system. The sample was laterally scanned with a 0.5 μm step size and with 200 ms exposure time per scanning point. Ninety projections were taken equally spaced over 180°. In the vertical direction, 10 slices equally spaced by 1 μm were collected. In-house developed Python routines based on the ASTRA library (van Aarle et al., 2016) were used for tomography analysis.

X-ray nanotomography (NCT):

NCT measurements were performed using the full field hard X-ray microscope at the beamline BL47XU at SPring-8, Japan providing an effective pixel size of 36.9 nm (Takeuchi, Uesugi, & Suzuki, 2009). Pieces of the cracked garnet were mounted in vacuum grease on a brass pin. All data sets were collected by rotating the samples 180° while recording 1,800 projections with an exposure time of 150 ms. The projection data were dark current (30 images collected before the data collection) and bright field (30 images collected before and after the tomography data) corrected. The truncated sinograms (since the field of view was smaller than the sample dimensions) were completed (Ravishankar, Kenneth, Stephen, & Daniel, 2005) and stripes were removed for ring artifact reduction (Münch, Trtik, Marone, & Stampanoni, 2009) before

reconstructing the 3D volume using the GridRec algorithm implemented in TomoPy (Gürsoy, De Carlo, Xiao, & Jacobsen, 2014).

Acknowledgements:

We grateful to the Swiss Light Source, Villigen, Switzerland for beamtime on the cSAXS beamline and to the Japan Synchrotron Radiation Research Institute for the allotment of beam time on beamline BL47XU of SPring-8 (Proposal 2018A1624). Support for travel and lodging at the synchrotron beamtime was provided by the Danish Agency for Science, Technology and Innovation via Danscatt. E. H. R. T. was supported by the Swiss National Science Foundation (SNSF) grant number 200020_169623. T. H. wishes to thank the Villum Foundation "Experiment" grant number 17387, and Independent Research Fund Denmark under project 1, for support.

References:

Abbaspour, N., Hurrell, R., & Kelishadi, R. (2014). Review on iron and its importance for human health. *Journal of Research in Medical Sciences, 19*(2), 164-174.

Aisen, P., Enns, C., & Wessling-Resnick, M. (2001). Chemistry and biology of eukaryotic iron metabolism. *International Journal of Biochemistry & Cell Biology, 33*(10), 940-959. doi:10.1016/s1357-2725(01)00063-2

Armstrong, F. A. J. (1957). The iron content of sea water. *Journal of the Marine Biological Association of the United Kingdom, 36*(3), 509-517. doi:10.1017/s0025315400025807

Bazylinski, D. A., & Frankel, R. B. (2004). Magnetosome formation in prokaryotes. *Nature Reviews Microbiology, 2*(3), 217-230. doi:10.1038/nrmicro842

Beard, J. L., Dawson, H., & Piñero, D. J. (1996). Iron Metabolism: a Comprehensive Review. *Nutrition Reviews, 54*(10), 295-317. doi:10.1111/j.1753-4887.1996.tb03794.x

Blakemore, R. (1975). Magnetotactic bacteria. *Science, 190*(4212), 377-379. doi:10.1126/science.170679

Canfield, D. E. (2005). The early history of atmospheric oxygen: Homage to Robert A. Garrels. *Annual Review of Earth and Planetary Sciences, 33*, 1-36. doi:10.1146/annurev.earth.33.092203.122711

Christiansen, B. C., Balic-Zunic, T., Petit, P. O., Frandsen, C., Mørup, S., Geckeis, H., . . . Stipp, S. L. S. (2009). Composition and structure of an iron-bearing, layered double hydroxide (LDH) – Green rust sodium sulphate. *Geochimica Et Cosmochimica Acta, 73*(12), 3579-3592. doi:10.1016/j.gca.2009.03.032

Czaja, A. D., Johnson, C. M., Beard, B. L., Roden, E. E., Li, W. Q., & Moorbath, S. (2013). Biological Fe oxidation controlled deposition of banded iron formation in the ca. 3770 Ma Isua Supracrustal Belt (West Greenland). *Earth and Planetary Science Letters, 363*, 192-203. doi:10.1016/j.epsl.2012.12.025

de Duve, C. (1990). PRELUDE TO A CELL. *The Sciences, 30*(6), 22-28. doi:10.1002/j.2326-1951.1990.tb02263.x

Diaz, A., Trtik, P., Guizar-Sicairos, M., Menzel, A., Thibault, P., & Bunk, O. (2012). Quantitative x-ray phase nanotomography. *Physical Review B, 85*(2), 020104. doi:10.1103/PhysRevB.85.020104

Dierolf, M., Menzel, A., Thibault, P., Schneider, P., Kewish, C. M., Wepf, R., . . . Pfeiffer, F. (2010). Ptychographic X-ray computed tomography at the nanoscale. *Nature, 467*(7314), 436-U482. doi:10.1038/nature09419

Drakesmith, H., & Prentice, A. M. (2012). Hepcidin and the Iron-Infection Axis. *Science, 338*(6108), 768. doi:10.1126/science.1224577

Dutkiewicz, A., Rasmussen, B., & Buick, R. (1998). Oil preserved in fluid inclusions in Archaean sandstones. *Nature, 395*(6705), 885-888. doi:10.1038/27644

Earhart, C. F. (2009). Iron Metabolism. In M. Schaechter (Ed.), *Encyclopedia of Microbiology (Third Edition)* (pp. 210-218). Oxford: Academic Press.

Farina, M., Esquivel, D. M. S., & de Barros, H. G. P. L. (1990). Magnetic iron-sulphur crystals from a magnetotactic microorganism. *Nature, 343*, 256. doi:10.1038/343256a0

Fedo, C. M., Whitehouse, M. J., & Kamber, B. S. (2006). Geological constraints on detecting the earliest life on Earth: a perspective from the Early Archaean (older than 3.7 Gyr) of southwest Greenland. *Philosophical Transactions of the Royal Society B: Biological Sciences, 361*(1470), 851-867. doi:10.1098/rstb.2006.1836

Ferrari, A. C., & Robertson, J. (2000). Interpretation of Raman spectra of disordered and amorphous carbon. *Physical Review B, 61*(20), 14095-14107. doi:10.1103/PhysRevB.61.14095

Gorelick, S., Vila-Comamala, J., Guzenko, V. A., Barrett, R., Salome, M., & David, C. (2011). High-efficiency Fresnel zone plates for hard X-rays by 100 keV e-beam lithography and electroplating. *Journal of Synchrotron Radiation, 18*, 442-446. doi:10.1107/s0909049511002366

Gürsoy, D., De Carlo, F., Xiao, X., & Jacobsen, C. (2014). TomoPy: a framework for the analysis of synchrotron tomographic data. *Journal of Synchrotron Radiation, 21*(Pt 5), 1188-1193. doi:10.1107/S1600577514013939

Hartmann, A., & Braun, V. (1981). Iron uptake and iron limited growth of Escherichia coli K-12. *Archives of Microbiology, 130*(5), 353-356. doi:10.1007/bf00414599

Hassenkam, T., Andersson, M. P., Dalby, K. N., Mackenzie, D. M. A., & Rosing, M. T. (2017). Elements of Eoarchean life trapped in mineral inclusions. *Nature, 548*(7665), 78. doi:10.1038/nature23261

Henrich, B., Bergamaschi, A., Broennimann, C., Dinapoli, R., Eikenberry, E. F., Johnson, I., . . . Schmitt, B. (2009). PILATUS: A single photon counting pixel detector for X-ray applications. *Nuclear Instruments & Methods in Physics Research Section a-Accelerators Spectrometers Detectors and Associated Equipment, 607*(1), 247-249. doi:10.1016/j.nima.2009.03.200

Holler, M., Diaz, A., Guizar-Sicairos, M., Karvinen, P., Farm, E., Harkonen, E., . . . Bunk, O. (2014). X-ray ptychographic computed tomography at 16 nm isotropic 3D resolution. *Scientific Reports, 4*. doi:10.1038/srep03857

Holler, M., Guizar-Sicairos, M., Tsai, E. H. R., Dinapoli, R., Muller, E., Bunk, O., . . . Aeppli, G. (2017). High-resolution non-destructive three-dimensional imaging of integrated circuits. *Nature, 543*(7645), 402-+. doi:10.1038/nature21698

Holler, M., Raabe, J., Wepf, R., Shahmoradian, S. H., Diaz, A., Sarafimov, B., . . . Vitins, M. (2017). OMNY PIN-A versatile sample holder for tomographic measurements at room and cryogenic temperatures. *Review of Scientific Instruments, 88*(11). doi:10.1063/1.4996092

Huang, X. J., Yan, H. F., Harder, R., Hwu, Y. K., Robinson, I. K., & Chu, Y. S. (2014). Optimization of overlap uniformness for ptychography. *Optics Express, 22*(10), 12634-12644. doi:10.1364/oe.22.012634

Kashefi, K., & Lovley, D. R. (2003). Extending the upper temperature limit for life. *Science, 301*(5635), 934-934. doi:10.1126/science.1086823

Kasting, J. F. (1993). Earths early atmosphere. *Science, 259*(5097), 920-926. doi:10.1126/science.11536547

Khai, T. V., Na, H. G., Kwak, D. S., Kwon, Y. J., Ham, H., Shim, K. B., & Kim, H. W. (2012). Influence of N-doping on the structural and photoluminescence properties of graphene oxide films. *Carbon, 50*(10), 3799-3806. doi:10.1016/j.carbon.2012.04.005

Larsen, M. B. B. S., Mackenzie, D. M. A., Caridad, J. M., Bøggild, P., & Booth, T. J. (2014). Transfer induced compressive strain in graphene: Evidence from Raman spectroscopic mapping. *Microelectronic Engineering, 121*, 113-117. doi:10.1016/j.mee.2014.04.038

Lepot, K., Addad, A., Knoll, A. H., Wang, J., Troadec, D., Béché, A., & Javaux, E. J. (2017). Iron minerals within specific microfossil morphospecies of the 1.88 Ga Gunflint Formation. *Nature Communications, 8*, 14890. doi:10.1038/ncomms14890

Luef, B., Fakra, S. C., Csencsits, R., Wrighton, K. C., Williams, K. H., Wilkins, M. J., . . . Banfield, J. F. (2013). Iron-reducing bacteria accumulate ferric oxyhydroxide nanoparticle aggregates that may support planktonic growth. *Isme Journal, 7*(2), 338-350. doi:10.1038/ismej.2012.103

Münch, B., Trtik, P., Marone, F., & Stampanoni, M. (2009). Stripe and ring artifact removal with combined wavelet — Fourier filtering. *Optics Express, 17*(10), 8567-8591. doi:10.1364/OE.17.008567

Neilands, J. B. (1974). *Microbial Iron Metabolism* (J. B. Neilands Ed.). New York and London: Academic press.

Nutman, A. P., & Friend, C. R. L. (2009). New 1:20,000 scale geological maps, synthesis and history of investigation of the Isua supracrustal belt and adjacent orthogneisses, southern West Greenland: A glimpse of Eoarchaean crust formation and orogeny. *Precambrian Research, 172*(3), 189-211. doi:10.1016/j.precamres.2009.03.017

Nutman, A. P., McGregor, V. R., Friend, C. R. L., Bennett, V. C., & Kinny, P. D. (1996). The Itsaq Gneiss Complex of southern West Greenland; the world's most extensive record of early crustal evolution (3900-3600 Ma). *Precambrian Research, 78*(1), 1-39. doi:10.1016/0301-9268(95)00066-6

Ohtomo, Y., Kakegawa, T., Ishida, A., Nagase, T., & Rosing, M. T. (2014). Evidence for biogenic graphite in early Archaean Isua metasedimentary rocks. *Nature Geoscience, 7*(1), 25-28. doi:10.1038/ngeo2025

Paulose, S., Raghavan, R., & George, B. K. (2016). Graphite oxide-iron oxide nanocomposites as a new class of catalyst for the thermal decomposition of ammonium perchlorate. *Rsc Advances, 6*(51), 45977-45985. doi:10.1039/c6ra06860j

Ravishankar, C., Kenneth, R. H., Stephen, R., & Daniel, R. B. (2005). *Artifact reduction in truncated CT using sinogram completion.* Paper presented at the Proc.SPIE.

Rosing, M. T. (1999). C-13-depleted carbon microparticles in > 3700-Ma sea-floor sedimentary rocks from west Greenland. *Science, 283*(5402), 674-676. doi:10.1126/science.283.5402.674

Rosing, M. T., & Frei, R. (2004). U-rich Archaean sea-floor sediments from Greenland - indications of > 3700 Ma oxygenic photosynthesis. *Earth and Planetary Science Letters, 217*(3-4), 237-244. doi:10.1016/s0012-821x(03)00609-5

Takeuchi, A., Uesugi, K., & Suzuki, Y. (2009). Zernike phase-contrast x-ray microscope with pseudo-Kohler illumination generated by sectored (polygon) condenser plate. *Journal of Physics: Conference Series, 186*, 012020. doi:10.1088/1742-6596/186/1/012020

Thibault, P., Dierolf, M., Menzel, A., Bunk, O., David, C., & Pfeiffer, F. (2008). High-resolution scanning x-ray diffraction microscopy. *Science, 321*(5887), 379-382. doi:10.1126/science.1158573

Thibault, P., & Guizar-Sicairos, M. (2012). Maximum-likelihood refinement for coherent diffractive imaging. *New Journal of Physics, 14*. doi:10.1088/1367-2630/14/6/063004

van Heel, M., & Schatz, M. (2005). Fourier shell correlation threshold criteria. *Journal of Structural Biology, 151*(3), 250-262. doi:10.1016/j.jsb.2005.05.009

van Aarle, W., Palenstijn, W. J., Cant, J., Janssens, E., Bleichrodt, F., Dabravolski, A., . . . Sijbers, J. (2016). Fast and flexible X-ray tomography using the ASTRA toolbox. *Optics Express, 24*(22), 25129-25147. doi:10.1364/oe.24.025129

Vargas, M., Kashefi, K., Blunt-Harris, E. L., & Lovley, D. R. (1998). Microbiological evidence for Fe(III) reduction on early Earth. *Nature, 395*(6697), 65-67.

Walker, J. C. G. (1987). Was the archean biosphere upside down. *Nature, 329*(6141), 710-712. doi:10.1038/329710a0

Whitehouse, M. J., Dunkley, D. J., Kusiak, M. A., & Wilde, S. A. (2019). On the true antiquity of Eoarchean chemofossils – assessing the claim for Earth's oldest biogenic graphite in the Saglek Block of Labrador. *Precambrian Research, 323*, 70-81. doi:10.1016/j.precamres.2019.01.001

Whitehouse, M. J., & Fedo, C. M. (2007). Chapter 7.1 Searching for Earth's Earliest Life in Southern West Greenland – History, Current Status, and Future Prospects. In M. J. van Kranendonk, R. H. Smithies, & V. C. Bennett (Eds.), *Developments in Precambrian Geology* (Vol. 15, pp. 841-853): Elsevier.

Whitehouse, M. J., & Fedo, C. M. (2007). Microscale heterogeneity of Fe isotopes in > 3.71 Ga banded iron formation from the Isua Greenstone Belt, Southwest Greenland. *Geology, 35*(8), 719-722. doi:10.1130/g23582a.1

Widdel, F., Schnell, S., Heising, S., Ehrenreich, A., Assmus, B., & Schink, B. (1993). Ferrous iron oxidation by anoxygenic phototrophic bacteria. *Nature, 362*(6423), 834-836. doi:10.1038/362834a0

Fig.1:

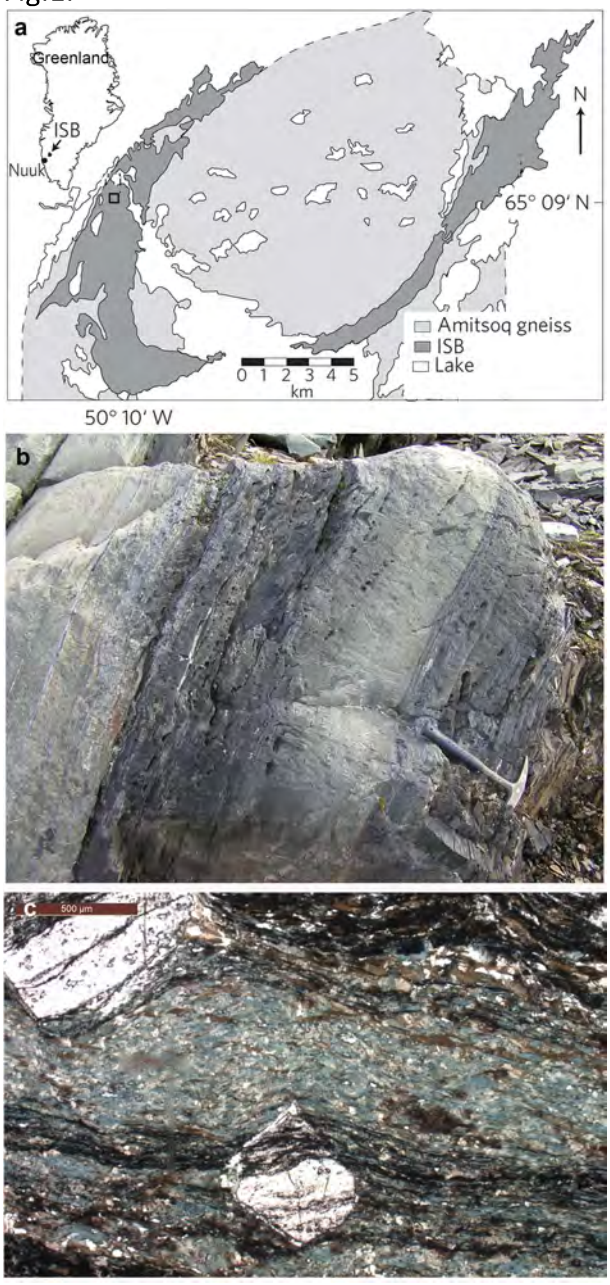

650

655

660

Fig 2:

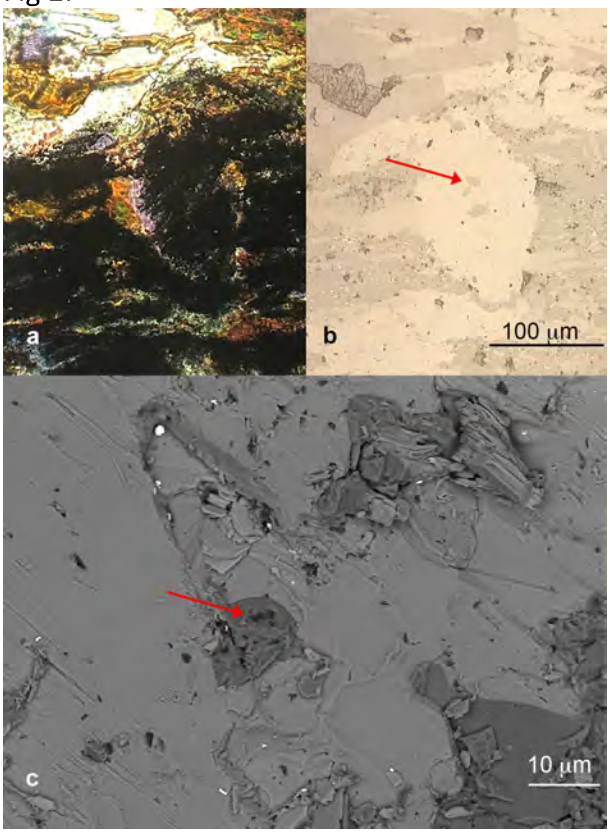

665 Fig. 3:

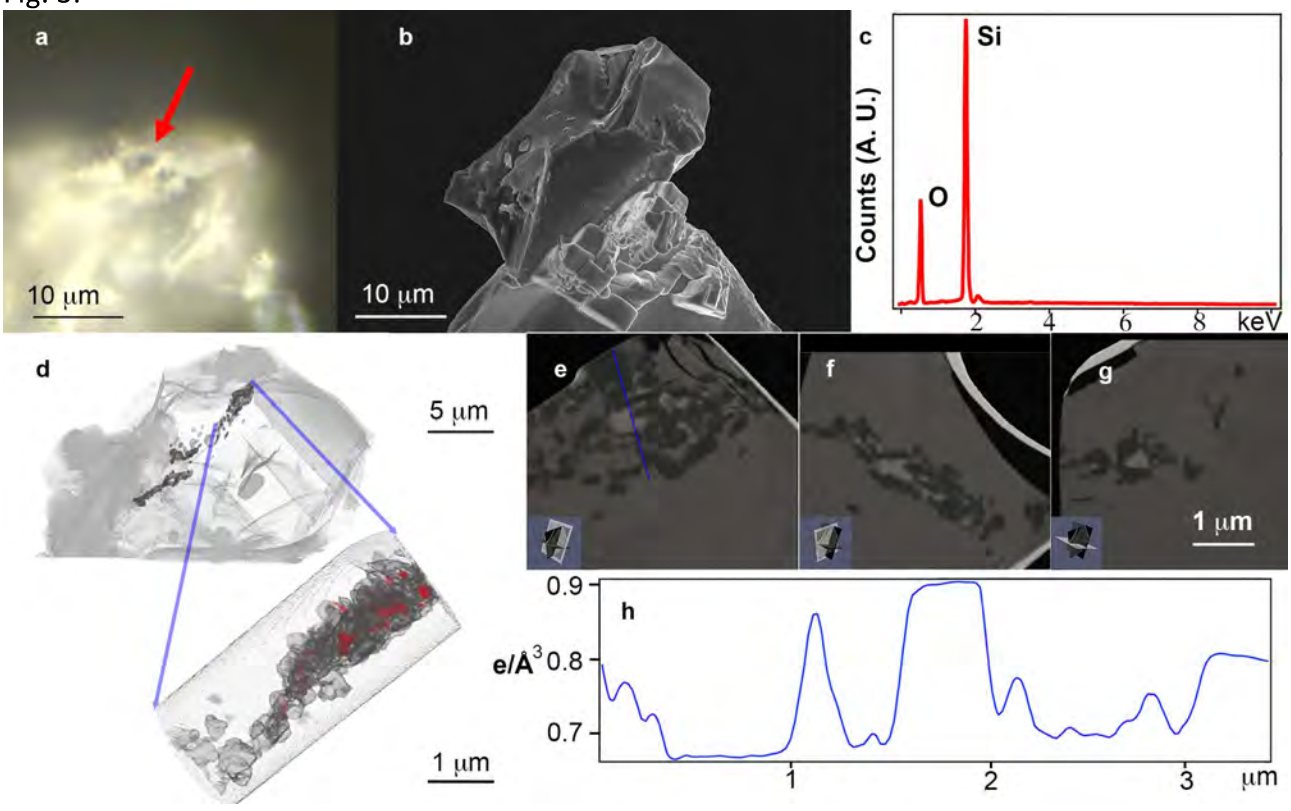

Fig. 4:

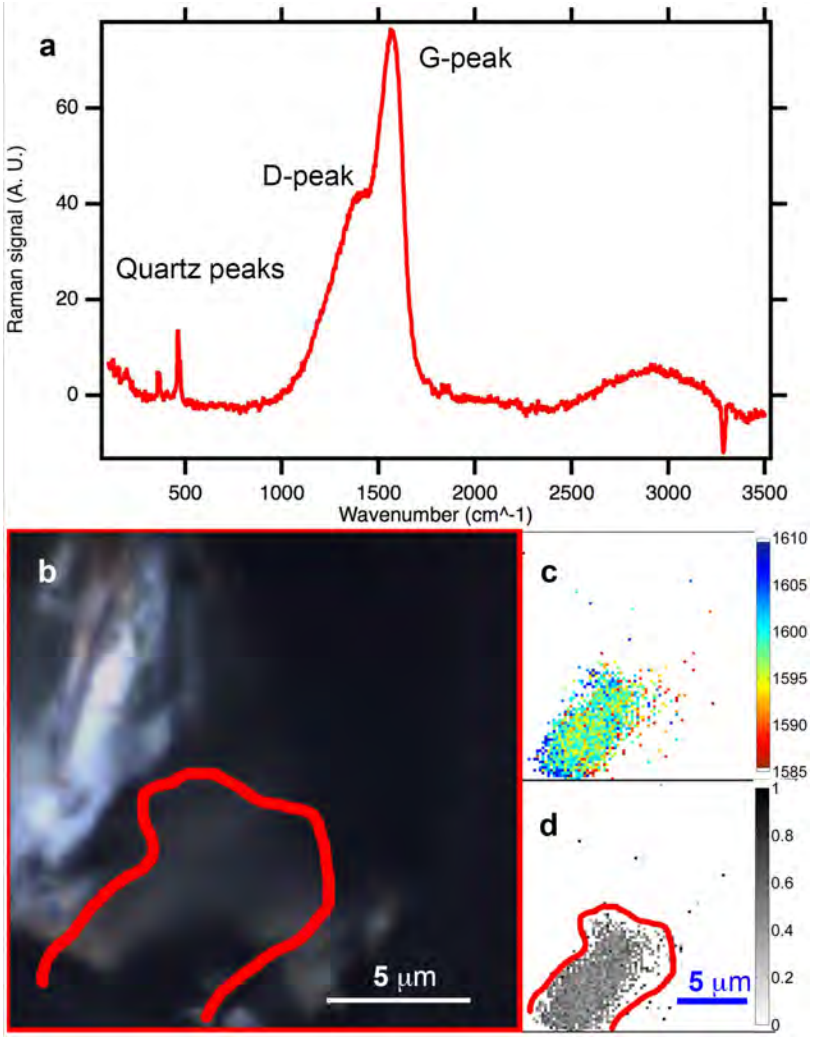

670

Fig. 5: